High-resolution carbon mapping on the million-hectare Island of Hawaii

Gregory P Asner[1*], R Flint Hughes[2], Joseph Mascaro[1], Amanda L Uowolo[2], David E Knapp[1], James Jacobson[1], Ty Kennedy-Bowdoin[1], and John K Clark[1]

Current markets and international agreements for reducing emissions from deforestation and forest degradation (REDD) rely on carbon (C) monitoring techniques. Combining field measurements, airborne light detection and ranging (LiDAR)-based observations, and satellite-based imagery, we developed a 30-meter-resolution map of aboveground C density spanning 40 vegetation types found on the million-hectare Island of Hawaii. We estimate a total of 28.3 teragrams of C sequestered in aboveground woody vegetation on the island, which is 56% lower than Intergovernmental Panel on Climate Change estimates that do not resolve C variation at fine spatial scales. The approach reveals fundamental ecological controls over C storage, including climate, introduced species, and land-use change, and provides a fourfold decrease in regional costs of C measurement over field sampling alone.

Front Ecol Environ 2011; doi:10.1890/100179

Voluntary markets and developing international agreements to credit nations for reducing emissions from deforestation and forest degradation (REDD) are increasingly relying on large-scale ecosystem monitoring. To support REDD activities, the Intergovernmental Panel on Climate Change (IPCC) issued guidelines to assist with carbon (C) assessment methodologies (Eggleston *et al.* 2006). These guidelines are organized into three tiers, each successively supporting increased accuracy and confidence to facilitate greater accountability, assurance, and potentially higher financial returns for monitoring and verifying C emissions. The most general approach (Tier I) is based on estimated biome-level variation in C stocks calculated from published values and other sources, which will undoubtedly generate major uncertainty and lower reliability for C stock and emissions information (Gibbs *et al.* 2007; Angelsen 2008). Although Tier I is designed to empower anyone to participate in programs requiring C accounting, there is substantial pressure to reach or exceed Tiers II and III, which provide increased detail on C stocks and emissions through the use of field-plot inventories, satellite mapping, and simulation models. Many REDD projects already call for much more detailed C mapping to reduce the potential for errors in performance reporting. Beyond REDD, improved C mapping is requisite to understanding the ecological processes that govern C dynamics as well as the human impacts on ecosystems.

Two kinds of data are required to effectively map aboveground C stocks across large, heterogeneous regions: (1) vegetation type and condition, including deforestation and degradation, and (2) the amount of C stored in different vegetation types ("C density" in megagrams [Mg] C per hectare). Various satellites measure vegetation cover and some aspects of vegetation structure (Chambers *et al.* 2007), but no existing satellite technology directly measures C density (GOFC-GOLD 2008). Traditionally, C density has been estimated by means of field-based inventory plots. Plots are important, but they are also expensive, time consuming, and inherently limited in geographic representativeness. Airborne mapping offers an effective alternative method for C assessment. The latest approaches, especially light detection and ranging (LiDAR) combined with field calibration plots, can reliably estimate aboveground C stocks over relatively large areas (Lefsky *et al.* 2002; Gonzalez *et al.* 2010), but even these approaches remain limited in terms of geographic coverage. To address this limitation, we integrated satellite-monitoring techniques with aircraft-based LiDAR mapping and a modest number of field plots to develop high-resolution C basemaps over spatially heterogeneous regions. Here we present a modification of the approach, originally developed by Asner (2009) and tested in the humid tropical forests of Amazonia (Asner *et al.* 2010), in an effort to cover a much wider range of ecosystems and vegetation types – from sparse shrublands to dense rainforest – on the one-million-hectare Island of Hawaii. We then focus on the ecological patterns revealed and on sources of uncertainty, and describe how a C basemap for Hawaii could be used to improve our understanding of C dynamics over time.

Methods

Study area

We selected the Island of Hawaii because its pronounced gradients of environmental, biotic, and land-use factors allowed us to test the efficacy of our approach across a

[1]*Department of Global Ecology, Carnegie Institution for Science, Stanford, CA* [*]*(gpa@stanford.edu);* [2]*Institute of Pacific Islands Forestry, USDA Forest Service, Hilo, HI*

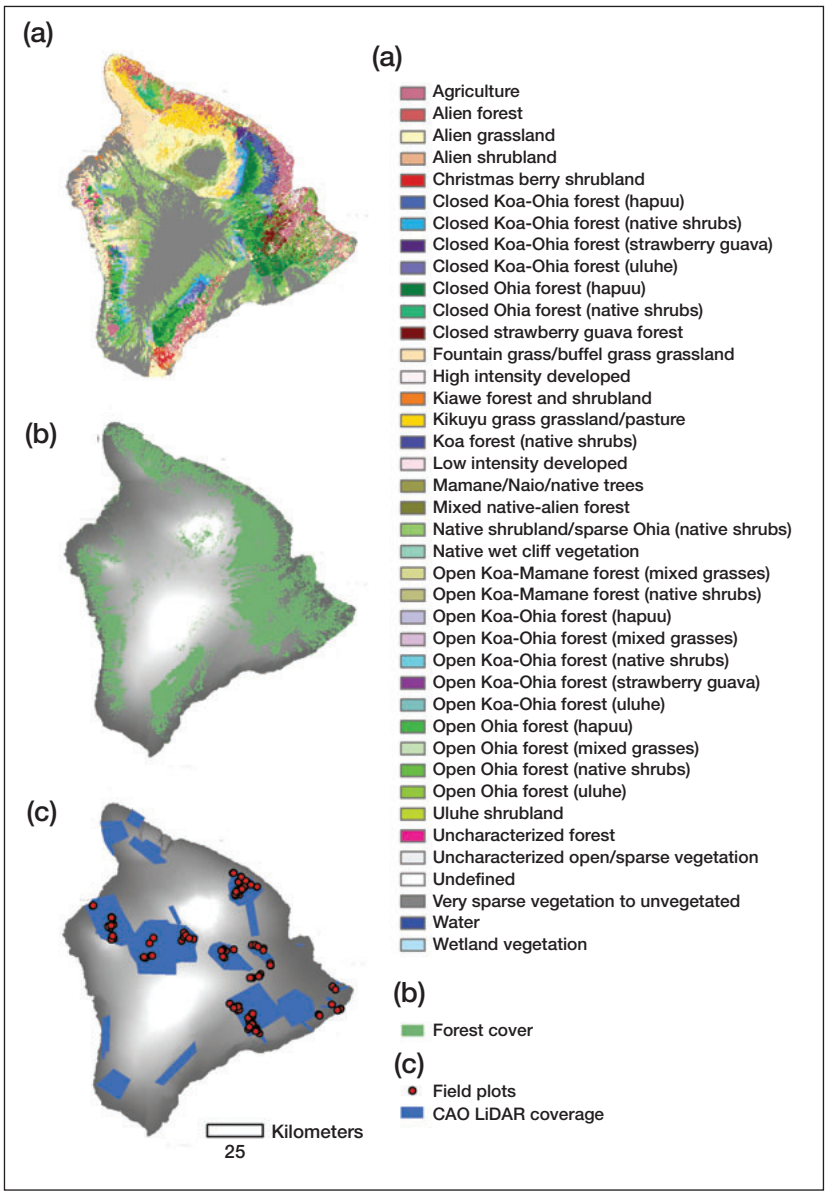

Figure 1. *(a) Vegetation stratification of Hawaii Island, based on the Hawaii Gap Analysis Program; (b) green area indicates forest cover detected by CLASlite; (c) blue areas indicate coverage of the Carnegie Airborne Observatory (CAO) LiDAR; red dots indicate location of field calibration plots.*

wide variety of ecosystems. Volcanic terrain, high mountains, and nearly constant northeasterly winds create an array of environmental conditions, with mean annual rainfall varying from 180 to 11 000 mm and mean temperatures ranging from 5° to 27° C (Armstrong 1983; Giambelluca *et al.* 1986). The Island of Hawaii contains 25 of the 35 Holdridge (1947) life zones (Asner *et al.* 2005), including alpine tundra, dry to wet sub-tropical forest, mesic woodlands and shrublands, and arid grasslands. These occur across a mosaic of different-aged lava flows, resulting in a diverse set of vegetation communities spanning a wide variety of developmental stages (Vitousek 2004).

We took four steps to produce a high-resolution C map of Hawaii: (1) whole-island characterization of vegetation type (eg *Metrosideros polymorpha* forest, *Acacia koa* forest, alien tree woodland) and condition (eg degraded, deforested) by combining a vegetation map with satellite-based data on forest cover; (2) stratified regional sampling of woody vegetation structure using airborne LiDAR; (3) conversion of LiDAR structural data to C estimates using a limited number of field calibration plots; and (4) integration of the regional maps with the airborne LiDAR data to yield island-wide aboveground C stock estimates.

Step 1: vegetation classification and satellite mapping

We used a vegetation map provided by the Hawaii Gap Analysis Program (GAP) to partition the landscape into ecologically relevant categories for subsequent airborne and field measurements (www.csc.noaa.gov/crs/lca/Hawaii.html; Figure 1a). Most vegetation maps, including the Hawaii GAP map, do not contain detailed information on vegetation condition, such as the degree and spatial extent of degradation. Yet mapping such detail is critical to maximize geographic information for REDD and similar programs. Degradation (eg caused by logging, fuelwood collection, fire) is particularly difficult to map because it often occurs diffusely over wide areas. The Carnegie Landsat Analysis System-Lite (CLASlite; http://claslite.ciw.edu/en/index.html) is an automated approach that maps both deforestation and forest degradation. We used CLASlite to map forest cover at 30-m spatial resolution, using a mosaic of nine Landsat and three Advanced Spaceborne Thermal Emission and Reflection (ASTER) images collected between February 2002 and January 2003. Details on CLASlite algorithms are available in Asner *et al.* (2009b).

The CLASlite map indicated that approximately 332 212 ha (32%) of Hawaii Island is forested, whereas 712 027 ha (68%) is non-forested (eg barren lava flows, open scrubland, grasslands, infrastructure; Figure 1b). Most of the island's forests are closed-canopy *M polymorpha* (28%), *A koa* (26%), and a mix of these two forest types (10%). Forests dominated by introduced species, including plantations, cover an additional 10% of the island.

Step 2: airborne LiDAR sampling

We collected LiDAR data with the Carnegie Airborne Observatory (CAO; Asner *et al.* 2007) over 253 744 ha, or about one-quarter of the island (Figure 1c; WebPanel

Panel 1. What is LiDAR?

LiDAR (light detection and ranging) systems emit high-frequency laser pulses at target landscapes and measure the elapsed time for pulses to return in order to calculate distance. Solid materials in forests, such as soil and wood, reflect the LiDAR pulses that contact them, but leaves are transmissive at typical LiDAR wavelengths of 900–1100 nanometers, and thus some LiDAR energy passes through foliage whereas some is reflected. As a result, LiDAR detects many levels of the forest canopy, and reproduces vertical structure in detail. We organized the laser returns into small rectangular cubes (5 m length, 5 m width, 1 m height) to examine the vertical distribution of vegetation, essentially creating a vertical histogram of laser returns in each 5 m × 5 m spatial cell. These histograms provided the underlying parameters (eg "canopy vertical profile") that we related to ground-based estimates of C density (Figure 2).

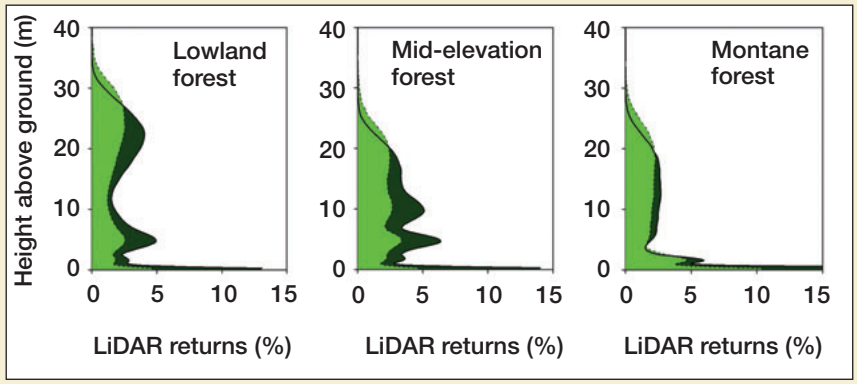

Figure 2. *Example of airborne LiDAR canopy vertical profiles of* Metrosideros polymorpha*-dominated lowland, mid-elevation, and montane forests. Dark green indicates the mean vertical profile, and light green indicates the standard deviation of the profiles in each forest type.*

1). Coverage strategically sampled the major vegetation types with and without woody vegetation cover, and across a wide range of climatic and soil conditions as indicated in step 1. We analyzed the resulting LiDAR data (Panel 1), and mapped vegetation height and vertical canopy profile using the techniques described by Asner *et al.* (2009a).

Step 3: linking field-based C density with LiDAR data

We established 126 field plots within the LiDAR coverage (Figure 1c), directing the plots to capture the maximum vegetation variability across Hawaii Island. We used LiDAR-derived canopy height maps to identify and sample the broadest structural range possible (ie short to tall canopies) within the most common vegetation types. In each 30-m-radius plot, we measured and identified all woody stems ≥ 5 cm in diameter at breast height (1.37 m above the ground; taxonomy follows that of Wagner *et al.* [1999]). Tree ferns (*Cibotium* spp) with stems ≥1.37 m tall were measured in a 9-m-radius plot nested within the larger plot. We used a combination of local and generalized allometric equations to estimate the aboveground C density of each plot (WebAppendix 1). We used a global positioning system receiver (Leica GS-50 with differential correction; Leica Geosystems Inc) to locate all plots within the LiDAR data.

To correlate plot and airborne data, we examined a suite of LiDAR metrics that capture forest structure, including height and the vertical profile of the canopy (WebPanel 2). LiDAR-derived mean canopy profile height (MCH, ie the centroid of the vertical canopy profile; Lefsky *et al.* 2002) consistently predicted aboveground C density among vegetation types in six distinct climatic regions, including canopies dominated by both native and introduced species. To assess the sensitivity of the LiDAR-to-C regression to the number of field plots measured, we tested the variability of the regression results by randomly excluding samples and recalculating the standard error of the estimate (SEE) and root mean square error (RMSE). This analysis suggested that no more than 20% (or 24) of the field plots were needed to stabilize the SEE and reduce the RMSE of the C-density estimates from LiDAR (WebPanel 3).

Step 4: integration of LiDAR and satellite data

Our final step combined the island-wide maps of vegetation type and forest cover with LiDAR-derived, aboveground C-density estimates. First, we calculated the median aboveground C density for undisturbed areas of each vegetation type. We then assigned these values to each 30-m pixel, after correcting for satellite-derived canopy fractional cover (WebPanel 4). For example, a pixel that appeared half-forested in our satellite analysis with CLASlite was assigned half of the LiDAR-derived median undisturbed aboveground C-density value for its vegetation type.

Results and discussion

Our LiDAR coverage of approximately one-quarter of the island revealed enormous variation in aboveground C density. Figure 3 depicts several sources of C-density variation for an area of lowland (upper right) to montane (lower left) rainforest. First, there is a background gradient of generally decreasing C density as elevation increases. Second, the colonization and spread of intro-

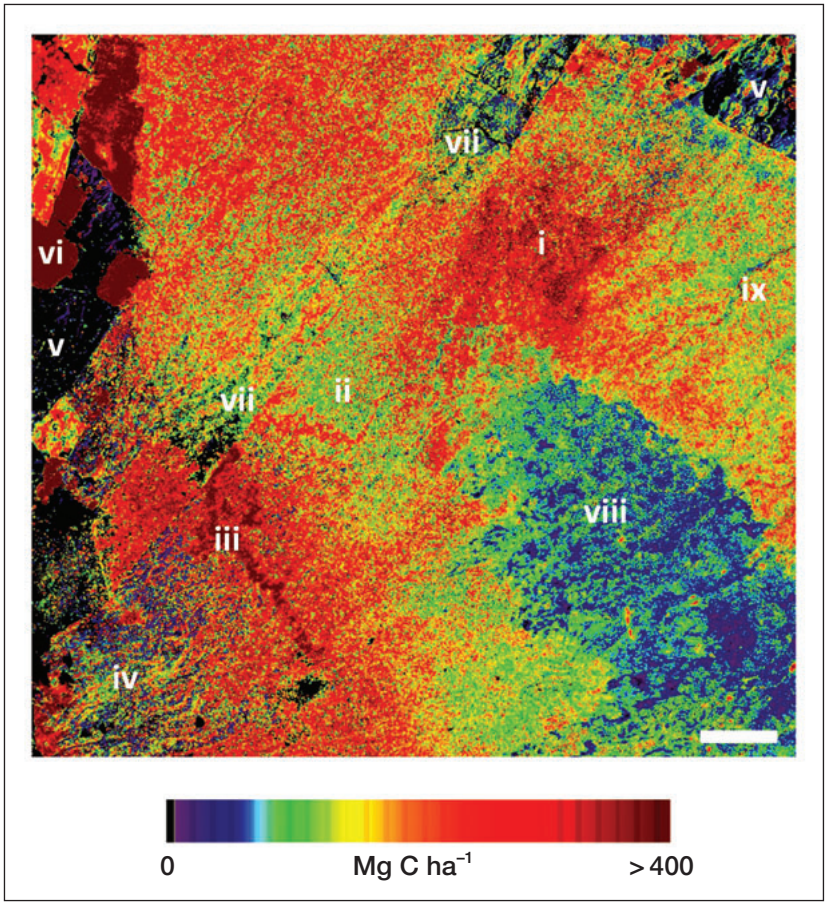

Figure 3. *This 100-km^2 subset shows the detail with which aboveground C densities can be mapped by airborne LiDAR. It also highlights many of the sources of variation in aboveground C stocks that occur on the Island of Hawaii: (i) old-growth native forest; (ii) native submontane forest; (iii) invasion by high-biomass species; (iv) secondary regrowth and old lava flows; (v) deforestation for cattle pasture; (vi) managed plantations; (vii) forest degradation from selective logging; (viii) terrain-mediated bog formation; and (ix) invasion by low-biomass species. The white bar indicates one km.*

duced species alter C density both positively and negatively, depending on the species involved (see Asner *et al.* 2009a). There are also areas of degraded forest resulting from selective logging operations and the conversion of forests to open woodlands and cattle pasture. These patterns are driven by decision making linked to road access, topography, wind direction, and other factors.

Our island-wide, high-resolution map also revealed detailed variation in aboveground C density and demonstrated the strong and often combined influence of soil and climatic conditions, as well as past and present land use, on aboveground C storage (Figure 4). The effects of substrate age and ecosystem development on C stocks are particularly evident. Basalt substrates range from days to several hundred thousand years old (Wolfe and Morris 1996), and the C map clearly tracks this variation. Areas of low C density (gray–blue) occur on young lava flows with little or no soil layer and very limited nutrients, such as the observed striations on the slopes of Mauna Loa. Areas of relatively high C density (yellow–red) occur on the eastern flanks of Mauna Kea, northeastern Kohala, and the southeastern and western flanks of Mauna Loa, where soils are generally older and well developed.

Climate also exerts strong control over C distributions in Hawaii. Prevailing winds from the northeast are forced upward by the volcanoes, producing high rainfall areas on windward exposures and resulting in high C density on the northeastern flanks of Mauna Loa, Mauna Kea, and Kohala. In contrast, drier, leeward portions of Hawaii exhibit low C densities, except in higher elevation areas where localized increases in precipitation occur. The marked decline in C density with the passage from the windward to the leeward side of Kohala clearly illustrates the role of precipitation – combined with past and current land use (eg ranching) – in determining C stocks. Interactions between climate and soil factors are also evident. A large area of high C density (the fin-shaped region on the windward side of Mauna Kea) occurs on well-developed, fertile soils with high precipitation, but encircles a large area of relatively low C values that is characterized by poorly drained soils supporting stunted forest and bog vegetation (also highlighted in Figure 3). Low temperatures and reduced precipitation strongly limit C stocks on the summits of Mauna Loa and Mauna Kea, which extend above the trade wind inversion layer (~2000 m; Giambelluca *et al.* 1986).

Past land use also has a profound influence on C patterns throughout Hawaii. The eastern lower reaches of Mauna Kea, long converted from forest to sugarcane (*Saccharum* spp) cultivation (Cuddihy and Stone 1990), exhibit an abrupt decline in C density below ~700 m elevation. The lower plains on the northwest flank of Mauna Kea also carry the marks of past land use. Here, extensive sandalwood (*Santalum* spp) forests were cleared during the 1800s (Barrera and Kelly 1974). This deforestation, combined with ranching and the spread of non-native, fire-prone grasses, has produced a landscape with very low C densities. The planting of introduced trees, which peaked at some four million trees per year during the Great Depression (circa 1920s to 1930s; Woodcock 2003), has also altered C densities across the island. The highest C densities occur in plantations at mid-elevations along the windward and, to a lesser extent, the leeward sides of Hawaii, and contain a median of 200 Mg C ha^{-1}.

The total aboveground C for the island was estimated at 28.3 teragrams, which is 56% lower than the value estimated by IPCC Tier I methods (WebPanel 5). The reason behind this difference is made clear by comparing our

high-resolution map with the Tier I map in Figure 4. First, we found that widespread forest degradation, which is distributed diffusely across the region, goes unaccounted for in the Tier I approach. Moreover, LiDAR sampling revealed much more variation in the C density of intact forests than that which is depicted in Tier I estimates. Tier I was not designed to resolve the effects of degradation or such detail in actual C densities, but the importance of doing so is made obvious here.

We compiled various sources of uncertainty from each step of the project (Table 1). Uncertainty in the Hawaii GAP vegetation map is unknown, but we noted various discrepancies during field validation exercises. These errors are non-random and often associated with a particular vegetation class in a particular location. Extensive field validation work indicated CLASlite errors of 3.7% for false-positive and 6.2% for false-negative detections of forest cover (including degraded forest). Plot-level biomass estimation errors range from 20 to 30% (Chave *et al.* 2004). Contributions from the LiDAR measurements are low as compared with other sources of error (< 4%), and the LiDAR-to-C conversion generated C-density prediction uncertainties of 18–23%. Apart from LiDAR-to-C errors in planted forests (WebPanel 2), these estimated uncertainties are comparable with – or even lower than – those found in much more geographically limited, ground-based methods when attempting to estimate C density. These errors are also nested within one another, and are not necessarily compounding (Asner *et al.* 2010; Table 1).

Although there are considerable up-front costs associated with deploying LiDAR platforms, the cost per hectare in this case was four orders of magnitude lower than that associated with field plots. For this one-million-hectare analysis – including LiDAR operation, data analysis, and satellite and LiDAR synthesis – the C-density map cost approximately $0.16 per ha to create. By comparison, the cost of field plots for just 39 ha of sampling, including personnel, supplies, and transportation, averaged about $1500 per ha. Field plots are essential to calibrate and validate LiDAR measurements to C density, but only a small number of plots are needed to accom-

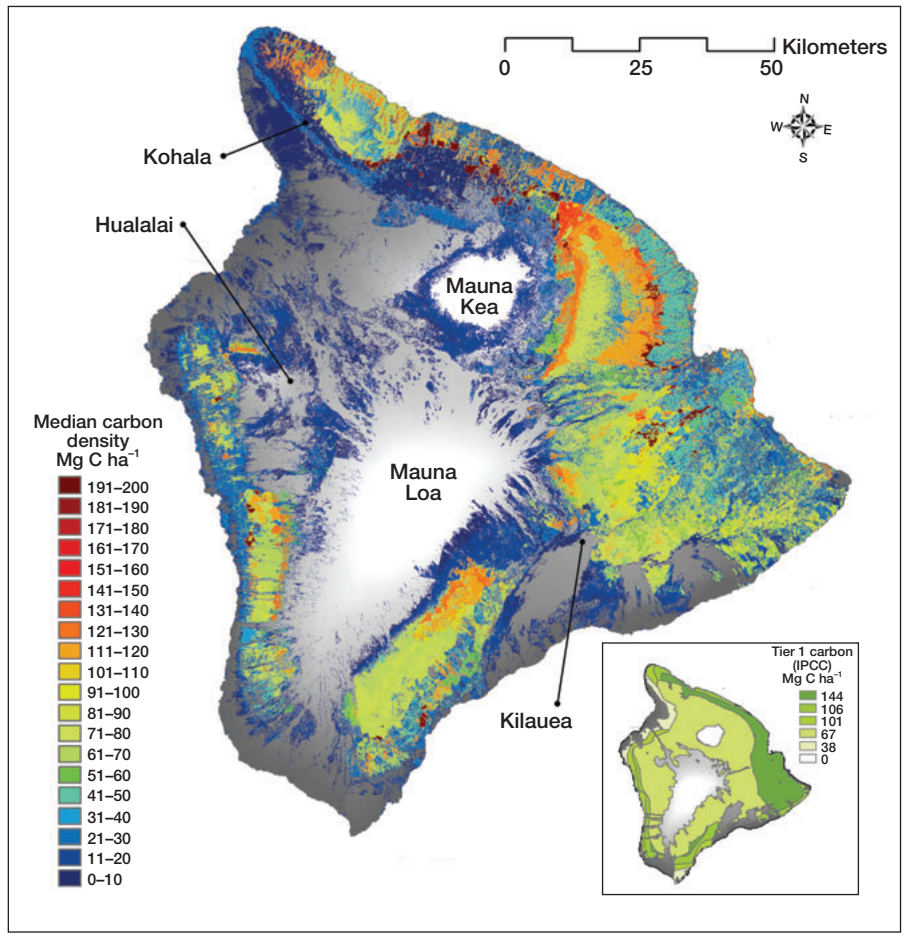

Figure 4. *Median values of aboveground C density throughout Hawaii Island, in units of Mg C ha^{-1}, mapped at 30-m spatial resolution through a combination of airborne LiDAR and satellite vegetation mapping. Inset shows aboveground C density estimated via IPCC Tier 1 data and methods (see WebPanel 5).*

Table 1. Overview of types of errors introduced through our approach

Step	*Error source*	*Uncertainty*	*Source*
(a) Vegetation map	Classification	Unknown but various discrepancies noted	HI-GAP Program
(b) Forest-cover map (CLASlite)	Fractional cover and classification	3.6–6.2%	This study
(c) LiDAR vegetation-structure metrics	Instrumentation analysis	< 4%	Asner *et al.* (2009a,b)
(d) Plot C estimation	Measurements, allometric models	20–30%	Chave *et al.* (2004)
(e) LiDAR-to-C conversion	Combined effects of (c) and (d) plus additional factors, including LiDAR sensitivity to biomass and LiDAR-to-plot co-location	18–23%	This study

plish this task. Indeed, our error analysis (WebPanel 3) suggested that fewer than 24 of our 126 plots would have been sufficient to calibrate the non-planted forests. Effectively sampling C-density variation at a landscape scale with field plots alone in an area as large as Hawaii Island would almost certainly prove too costly. Another factor to consider is the amount of LiDAR sampling required to assess C-density distributions for each vegetation type. We purposely over-sampled to facilitate analysis but, in the end, found that a 1% sampling of vegetation types was sufficient in most cases. However, the project benefitted from the pre-existence of a vegetation map, which may not always be available.

LiDAR also provides unique opportunities for C accounting and research in remote areas that may be exceedingly difficult to access on the ground. On Hawaii Island, for example, we measured C density in the Hakalau National Wildlife Refuge, which is closed to the public and includes many endangered bird and plant species (WebPanel 6). Nearby, on lands dominated by old-growth *M polymorpha* forest, we measured the largest standing C density on the entire island. With future LiDAR flights, it will be possible to study these ancient forests without setting foot in them, providing new insights into old-growth forest dynamics.

A key advantage of our approach is that LiDAR will be needed only in a limited capacity to monitor future C stocks and emissions. After the development of a high-resolution C basemap, it will then be straightforward to monitor the effects of future deforestation and degradation through the use of freely available satellite data (Asner 2009). With many types of satellite imagery (eg Landsat), one can simply subtract C from the C basemap when forest losses are detected. This approach could support end-users from many sectors – including science, conservation, and resource management – to monitor emissions over time, providing transparent information flow to support C accounting and REDD-type projects and programs.

Acknowledgements

We thank I Joaquin, M Joaquin, R Loo, A Cortes Jr, T Gaoteote, L Nakagawa, and G Sanchez for assistance with field-plot data collection. We also thank Hawaii Volcanoes National Park and the Hawaii State Division of Forestry and Wildlife for site access. This study was supported by the Gordon and Betty Moore Foundation. The Carnegie Airborne Observatory is made possible by the WM Keck Foundation, the Gordon and Betty Moore Foundation, and William Hearst III.

References

Angelsen A. 2008. Moving ahead with REDD: issues, options and implications. Bogor, Indonesia: Center for International Forestry Research (CIFOR).

Armstrong RW (Ed). 1983. Atlas of Hawaii, 2nd edn. Honolulu, HI: University of Hawaii Press.

Asner GP. 2009. Tropical forest carbon assessment: integrating satellite and airborne mapping approaches. *Environ Res Lett* **4**: 034009.

Asner GP, Elmore AJ, Hughes FR, *et al.* 2005. Ecosystem structure along bioclimatic gradients in Hawaii from imaging spectroscopy. *Remote Sens Environ* **96**: 497–508.

Asner GP, Hughes RF, Varga TA, *et al.* 2009a. Environmental and biotic controls over aboveground biomass throughout a tropical rain forest. *Ecosystems* **12**: 261–78.

Asner GP, Knapp DE, Balaji A, and Paez-Acosta G. 2009b. Automated mapping of tropical deforestation and forest degradation: CLASlite. *J Appl Remote Sens* **3**: 033543.

Asner GP, Knapp DE, Kennedy-Bowdoin T, *et al.* 2007. Carnegie Airborne Observatory: in-flight fusion of hyperspectral imaging and waveform light detection and ranging (LiDAR) for three-dimensional studies of ecosystems. *J Appl Remote Sens* **1**: 013536.

Asner GP, Powell GVN, Mascaro J, *et al.* 2010. High-resolution carbon stocks and emissions in the Amazon. *P Natl Acad Sci USA* **107**: 16738–42.

Barrera Jr W and Kelly M. 1974. Archaeological and historical surveys of the Waimea to Kawaihae Road corridor, Island of Hawaii. Hawaii Historic Preservation Report 74-1. Honolulu, HI: BP Bishop Museum.

Chambers JQ, Asner GP, Morton DC, *et al.* 2007. Regional ecosystem structure and function: ecological insights from remote sensing of tropical forests. *Trends Ecol Evol* **22**: 414–23.

Chave J, Chust G, Condit R, *et al.* 2004. Error propagation and scaling for tropical forest biomass estimates. In: Malhi Y and Phillips O (Eds). Tropical forests and global atmospheric change. London, UK: Oxford University Press.

Cuddihy LW and Stone CP. 1990. Alteration of native Hawaiian vegetation: effects of humans, their activities and introductions. Honolulu, HI: University of Hawaii Press.

Eggleston S, Buendia L, Miwa K, *et al.* (Eds). 2006. 2006 IPCC guidelines for national greenhouse gas inventories. Hayama, Japan: Institute for Global Environmental Strategies.

Giambelluca TW, Nullet MA, and Schroeder TA. 1986. Rainfall atlas of Hawaii. Honolulu, HI: Department of Land and Natural Resources, State of Hawaii.

Gibbs HK, Brown S, Niles JO, and Foley JA. 2007. Monitoring and estimating tropical forest carbon stocks: making REDD a reality. *Environ Res Lett* **2**: 1–13.

GOFC-GOLD (Global Observation of Forest and Land Cover Dynamics). 2008. Reducing greenhouse gas emissions from deforestation and degradation in developing countries: a sourcebook of methods and procedures for monitoring, measuring and reporting. Edmonton, Canada: GOFC-GOLD.

Gonzalez P, Asner GP, Battles JJ, *et al.* 2010. Forest carbon densities and uncertainties from Lidar, QuickBird, and field measurements in California. *Remote Sens Environ* **114**: 1561–75.

Holdridge LR. 1947. Determination of world plant formations from simple climate data. *Science* **105**: 367–68.

Lefsky MA, Cohen WB, Parker GG, and Harding DJ. 2002. Lidar remote sensing for ecosystem studies. *BioScience* **52**: 19–30.

Vitousek PM. 2004. Nutrient cycling and limitation: Hawaii as a model system. Princeton, NJ: Princeton University Press.

Wagner WL, Herbst DR, and Sohmer SH. 1999. Manual of the flowering plants of Hawaii. Honolulu, HI: University of Hawaii Press and Bishop Museum Press.

Wolfe EW and Morris J. 1996. Geologic map of the island of Hawaii. Reston, VA: US Geological Survey.

Woodcock D. 2003. To restore the watersheds: early twentieth-century tree planting in Hawaii. *Ann Assoc Am Geogr* **93**: 624–35.

GP Asner *et al.* – Supplemental information

WebPanel 1

Airborne light detection and ranging (LiDAR) flights were conducted in two different modes: (1) High-resolution: 1000 m above ground level, 0.56 m LiDAR spot spacing, 24 degree field of view, 70 kHz pulse repetition frequency; and (2) Low-resolution: 2000 m above ground level, 1.12 m LiDAR spot spacing, 30 degree field of view, 50 kHz pulse repetition frequency. For both flight modes, the aircraft maintained a ground speed of less than 85 knots. LiDAR spatial error was less than 0.15 m vertically and less than 0.36 m horizontally (RMSE). Flights were planned to sample forest (and other) vegetation using parallel flight lines with 50% overlap to ensure full and consistent coverage.

WebPanel 2

We tested various LiDAR metrics, including MCH (mean canopy profile height), QMCH (quadratic mean canopy height), and CH (top-of-canopy height) (described by Lefsky *et al.* 2002). Within the footprint of one field plot (a 30-m radius circle), each LiDAR metric was computed at 5-m spatial resolution and 1-m vertical resolution. In each case, LiDAR data strongly predicted aboveground C density, although separate models were required to account for variation in natural forests (both native and introduced) and planted forests (WebFigures 1 and 2). We note that errors in the prediction of carbon density among planted forests substantially increase at higher values of any LiDAR metric tested (WebFigure 1). This elevated degree of heteroskedasticity in planted forests appears to be due to variations in stocking rate

or basal area among plantations with similar height and/or vertical canopy profile structure. The LiDAR metrics used in this study are more sensitive to variations in canopy height and vertical profile and not basal area.

WebPanel 3

To assess the sensitivity of the LiDAR-to-C relationship to the number of field plots measured, we tested the variability of the regression results by randomly leaving multiples of 5% of the samples out of the regression and calculating the standard error of the estimate (SEE) for each resulting regression equation. We repeated this 1000 times, with each run removing and adding back a random set of six field plots. This allowed for characterization of the error inherent in the model with larger sample numbers. The SEE initially increases as the sample number increases in the regression model (WebFigure 3). It reaches a plateau at about 12, suggesting that additional samples do not significantly improve the relationship between the LiDAR metric and aboveground C. The predictive power of the regression was then assessed by calculating the root mean squared error (RMSE) of a set of independent (n = 7) samples, which were not used in developing the regression equation. We repeated this analysis 1000 times with regression models that increased in sample size from 5% to 95% of the original data set. WebFigure 3 (red line) indicates an initial rapid decline in RMSE from 38 Mg C ha^{-1} when 5% (7 plots) are used in the regression to 31 Mg C ha^{-1} when 20% (24 plots) are used. Thereafter, as the number of plots is increased, the predictive error only decreases to 30.5 Mg C ha^{-1}.

WebPanel 4

Median LiDAR-based values were extracted for undisturbed canopies in each vegetation class. This was made possible by excluding recently deforested and degraded areas mapped with CLASlite from the LiDAR data. Aboveground C density (ACD) was then mapped at 30-m resolution in each vegetation class by applying the median undisturbed ACD down-scaled using the fractional canopy cover from CLASlite:

$$ACD(x,y)_{veg(z)} = ACDmedian_{veg(z)} * PV(x,y)_{CLASlite} \quad (1)$$

where $ACD(x,y)_{veg(z)}$ is the aboveground C density of pixel x,y in vegetation type z; ACDmedian is the median ACD of undisturbed forest derived from airborne LiDAR mapping of vegetation type z; and $PV(x,y)_{CLASlite}$ is the fractional (0.0-1.0) cover of photosynthetic vegetation of pixel x,y derived from CLASlite. PV fraction in forests is equivalent to canopy fractional cover, which is highly correlated with canopy damage, disturbance and degradation (Asner *et al.* 2005; Asner *et al.* 2006; Broadbent *et al.* 2008). To provide maps of ACD uncertainty by vegetation type and condition with respect to degradation, the entire procedure was repeated using the standard deviation of LiDAR-based ACD values for undisturbed canopies in each vegetation type.

WebPanel 5

We compared our high-resolution mapping approach to the standard IPCC Tier-I analysis of aboveground C stocks for Hawaii Island. To identify land-cover type, Holdridge Life Zones for the Island of Hawaii (Asner *et al.* 2005) were reclassified to Global Ecological Zones (GEZ) according to the methodology developed for the FAO's Forest Resources Assessment 2000 (FAO 2000). Areas of bare exposed rock were cut from the GEZ polygons using a land-cover map provided the state of Hawaii. The GEZ were then stratified in a geographic information system by a land-cover mask generated from a globally available, low-resolution land cover dataset (1000 m) (GLC 2000). To create the land-cover mask, we reclassified the data as forest or non-forest using classes of GLC 2000 (Gibbs *et al.* 2007). For our study area, these classes were limited to "broadleaved, evergreen tree cover" and "mosaic: tree cover/other natural vegetation" (GLC 2000). Aboveground C density was calculated for forested areas by GEZ using generic IPCC values (IPCC 2006).

WebPanel 6

Airborne LiDAR provides a non-intrusive means to assess forest structure and aboveground carbon density in protected or remote areas, such as the Hakalau National Wildlife Refuge, which is closed to the public to protect several critically endangered birds and plants (WebFigure 4).

WebAppendix 1. Supplemental field methods and allometric models

General approach

The IPCC recommends that species-specific variation be incorporated into estimates of aboveground biomass (AGB) where possible (IPCC 2006). For a given tree, a species-specific diameter-to-AGB allometric equation is preferable to a general model based on multiple species. However, the high diversity of tropical forests precludes the possibility of constructing species-specific models for all species, and thus general models are required. Chave *et al.* (2005) produced six general models for three forest types: wet (> 3500 mm mean annual precipitation), moist (1500–3500), and dry (< 1500). For each forest type, the "Chave 1" model requires inputs of diameter, wood density, and height. Another model ("Chave 2") requires only inputs of diameter and wood density. In either case, species-specific wood density can be sampled or taken from the literature. While height measurements are preferred, height can also be estimated from diameter using allometric models correlating diameter to height, and this method of correcting for height variation has shown to improve AGB estimates dramatically (Nogueira *et al.* 2008).

We used a hierarchical approach to estimate AGB, accounting for as much species-specific and regional variation as possible with a 4-tier system. At the first tier, we used locally derived species-specific diameter-to-AGB models for seven common species, including the three most abundant species in the study region: *Metrosideros polymorpha*, *Psidium cattleianum*, and *Morella faya* (WebTable 1). At the second tier, we used genera- or life-form-specific models (WebTable 1). Models for tree ferns and dead trees require height inputs which were measured in the field using a combination of diameter and height measurements. In most

cases, the diameter-to-AGB models had limited diameter ranges (due to limitations of the harvest datasets upon which the models were based), and the AGB of larger individuals was estimated using the methods described for general Chave *et al.* models. At the third tier, we estimated AGB using general Chave *et al.* models (according to forest type classifications described below), coupled with locally derived species-, or genera-specific diameter-to-height models (WebTable 2). Finally, at the fourth tier, we used a combination of general Chave *et al.* models and general diameter-to-height models (WebTable 2). Where the Chave *et al.* models were employed, we used a combination of locally sampled wood density estimates and values taken from a global wood density database (Chave *et al.* 2009). If no wood density estimate was available for a given species, we used a genera-specific value. If this was not available, we used a default value of 0.50 g cm^{-3}. A species-level accounting of the assignment of diameter-to-AGB models, diameter-to-height models, and wood density values was used to produce plot-level AGB estimates (WebTable 3).

Diameter-to-height models

We measured the diameter and height of 3362 individual trees (39 species) and 3356 individual tree ferns (4 species) on Hawaii Island using a combination of tape measurements, laser range finders, and clinometers. We sampled in wet, moist, and dry forest types in three distinct physiographic provinces: Puna (wet, moist), Laupahoehoe (moist), and Pu'u Wa'a Wa'a (PWW; dry). We sampled lowland areas in Puna, primarily in forest reserves with nutrient-limited basalt lava flows (50 – 3000 years old, with most flows < 200 years old), where mean annual precipitation (MAP) ranges from 2000 to 4000 mm. We sampled mid-elevation zones in the

Laupahoehoe section of the Hilo Forest Reserve, characterized by nutrient-rich, clayey soils derived from weathered basalt flows (20,000 and 65,000+ years old) with MAP ranges from 2500–3500 mm. We also sampled low to mid elevation areas across the dry leeward PWW unit of the Hawaii Experimental Tropical Forest. Here relatively young lava flows range in age from 200 to 10000 years old; MAP from 250 – 1000 mm. Native forests are dominated by *Metrosideros polymorpha*, with co-dominance by *Acacia koa* in Laupahoehoe and PWW, while stands of introduced trees are dominated primarily by *Falcataria moluccana*, *Psidium cattleianum*, and *Prosopis pallida* among many others (Litton *et al.* 2006; Mascaro *et al.* 2008; Zimmerman *et al.* 2008; see also www.csc.noaa/gov/crs/lca/hawaii.html).

Of the 41 species in our diameter-to-height dataset, 10 species were encountered infrequently and did not generate species-specific diameter-to-height relationships, while 27 species that were confined to either wet or dry regions generated significant models (WebTable 2). For the four remaining species, we compared relationships among provinces and found that they did not fundamentally differ between the wet provinces of Puna and Laupahoehoe; however, the relationships differed strongly between the wet region (Puna + Laupahoehoe) and the dry region (PWW) (WebFigure A1). Thus, for these species we generated both wet and dry diameter-to-height models. We generated regional diameter-to-height models from our full tree datasets (e.g., without tree ferns) for both the wet and dry regions, as well as a genera-specific model for *Cibotium* spp that served as a general tree fern model. We also developed genera-specific *Eucalyptus* relationships, and excluded *Eucalyptus* data from our general tree models because these species grow significantly taller than all other species on Hawaii (Wagner *et al.* 1999).

For each of the 39 total models, we compared four different types of allometric relationships between tree diameter and height. We first applied a linear fit to ln-transformed diameter and height of the form:

$$\ln(H) = a + b \ln(D) \quad (1)$$

where H = height (m), D = diameter (cm) at 1.37 m from the ground or above buttresses, and a and b are regression coefficients. We next applied a quadratic fit to ln-transformed diameter and height of the form:

$$\ln(H) = a + b \ln(D) + c \ln(D)^2 \quad (2)$$

where c is an additional regression coefficient. Equations 1 and 2 were back-transformed, and in each case a correction factor was calculated to account for the back-transformation of the regression error (Baskerville 1972). We also applied a non-linear exponential rise-to-maximum (ERTM) fit to diameter and height of the form:

$$H = a (1 – \exp(–b + D)) \quad (3)$$

where a and b are regression coefficients. Finally, we considered a variant of Eq. 3 that includes an additional scaling coefficient:

$$H = c + a (1 – \exp(–b + D)) \quad (4)$$

The relative fit of each equation was compared, and a best fit was determined based on the ability of the equation to consistently predict height across the range of diameters sampled (as assessed by a visual examination of the residuals) and on the goodness-of-fit (r^2, p-value, and mean squared error). In cases where multiple models were comparable in their predictive power, ERTM models were given preference, as the ERTM relationship is thought to be an accurate mathematical representation of tree growth (Niklas 1995). However, we observed

that ERTM models often departed substantially from the observed data at small diameters (e.g., where individual points have the least influence on goodness-of-fit), and in such cases ERTM models were rejected. All model fits were preformed in SigmaPlot 10.0 (Systat Software Inc, San Jose, CA, 2006).

Classification of forest types

The Chave *et al.* (2005) suite of general models requires classification of forest types according to three climate zones: wet, moist, and dry. Approximations of mean annual precipitation (MAP) and mean annual temperature (MAT) were derived from GIS layers provided by the state government of Hawaii (Giambelluca *et al.* 1986; www.ncdc.noaa.gov.html). These layers were intersected using ArcGIS 9.3 (2007) to produce a map of the combined classes (WebTable 4).

WebTable 1. Diameter-to-biomass models used to estimate aboveground biomass (AGB). Assignment of models to particular species and diameter ranges can be found in WebTable 3. Omitted descriptive statistics were not provided in the primary source. D is diameter (cm) at 1.37 m from the ground or above buttress; BD is diameter (cm) around the base; H is height (m); ρ is wood density (g cm^{-3}); regions of origin are (1) Hawaii, (2) Canary Islands, (3) Peru, and (4) Mexico; model types are (1) linear, (2) power-law, and (3) multivariable.

#	species	Origin	Type	Diameter-to-AGB model (calculates AGB in kg)	r^2	Min D (cm)	Max D (cm)	n	Ref[1]
1	*Acacia koa*	1	1	exp(-2.3270+2.3500*ln(D))*1.0171	0.99	1.5	30.0		1
2	*Dodonaea viscosa*[2]	1	2	$0.13*(BD*10)^{2.55})/1000$	0.95	0.5	2.9	20	2
3	*Metrosideros polymorpha*	1	1	exp(-2.1311+2.5011*ln(D))*1.0671	0.98	1.8	33.0	24	3
4	*Morella faya*[3]	2	1	exp(-1.3412+2.1628*ln(D))	0.99				4
5	*Prosopis pallida*[2]	3	1	exp(-1.0188+2.1079*ln(BD))*1.0378	0.92	12.7	48.7	17	5
6	*Psidium cattleianum*	1	1	exp(-1.9096+2.5763*ln(D))*1.0084	0.99	1.7	18.2	19	6
7	*Fraxinus uhdei* (wood)[3,4]	1	1	exp(-2.7339+2.5974*ln(D))	0.99		91.6		7
7	*Fraxinus uhdei* (leaves)[3,4]	1	1	exp(-5.921+2.243*ln(D))	0.81		91.6		7
8	General dead trees < 10 cm	4	1	$exp(4.6014+1.1204*ln(D^2))*1.11*10^{-3}$	0.95		9.9		8
9	General dead trees ≥ 10 cm	n/a[5]	3	$PI*(D/2)^2*H*100*0.5/1000$		n/a[5]			9
10	General tree ferns	n/a[5]	3	$PI*(D/2)^2*H*100*\rho/1000$		n/a[5]			9

[1](1) Scowcroft and Fujii unpublished data, (2) Litton and Kauffman (2008), (3) CM Litton unpublished data, (4) Aboal *et al.* (2005), (5) raw harvest data from Padron and Navarro (2004), (6) RF Hughes unpublished data, (7) D Rothstein and PM Vitousek unpublished data, (8) Hughes *et al.* (1999), (9) RF Hughes unpublished data.

[2]Model estimates AGB based on basal diameter (cm).

[3]A correction factor is incorporated.

[4]Results of models for wood and leaf tissues were combined to estimate total AGB.

[5]AGB for dead trees and tree ferns was estimated using the volume of a cylinder, with measurements of tree diameter, height, and wood density.

WebTable 2. Species-specific and general diameter-to-height models used to estimate height according to the assigned model numbers in WebTable 3. *D* is diameter (cm) at 1.37 m from the ground or above buttress; H is height (m); region (Reg) is either dry (D), wet (W), or island-wide (I); model types are (1) linear, (2) quadratic, (3) exponential rise-to-maximum, and (4) exponential rise-to-maximum with an additional scaling coefficient.

#	species	Reg	Type	Diameter-to-height model (calculates H in m)	r^2	Min D (cm)	Min H (m)	Max D (cm)	Max H (m)	n
1	*Acacia koa*	D	2	exp(0.0367+0.9886*ln(D)-0.0871*ln(D)^2)*1.0219	0.82	2.2	2.1	130.2	20.4	115
2	*Acacia koa*	W	2	exp(0.1795+1.0160*ln(D)-0.0800*ln(D)^2)*1.0156	0.84	1.7	2.4	140.4	28.0	198
3	*Antidesma platyphyllum*	W	4	1.1240+8.5503*(1-exp(-0.1079*D))	0.80	1.1	1.8	13.7	8.9	60
4	*Casuarina equisetifolia*	W	3	28.6202*(1-exp(-0.0517*D))	0.80	2.3	3.3	74.8	35.4	47
5	*Cecropia obtusifolia*	W	3	23.0165*(1-exp(-0.0678*D))	0.87	0.9	1.7	35.5	24.4	85
6	*Cheirodendron trigynum*	W	3	12.6477*(1-exp(-0.1365*D))	0.63	1.3	2.0	45.0	17.9	91
7	*Cibotium chamissoi*	I	1	exp(0.6457+1.5932*ln(D))*1.2763/100	0.74	1.7	0.0	47.5	6.3	174
8	*Cibotium glaucum*	I	1	exp(-0.6277+1.6910*ln(D))*1.1386/100	0.72	2.0	0.0	58.0	6.0	2142
9	*Cibotium menziesii*	I	1	exp(-0.6549+1.8683*ln(D))*1.1705/100	0.72	2.8	0.1	65.2	9.0	856
10	*Cibotium* spp	I	1	exp(-0.4531+1.6955*ln(D))*1.2071/100	0.67	1.7	0.0	65.2	9.0	3172
11	*Coprosma* spp	W	3	10.2252*(1-exp(-0.2257*D))	0.57	1.0	2.2	19.6	14.8	108
12	*Diospyros sandwicensis*	D	3	6.0846*(1-exp(-0.1010*D))	0.29	9.2	2.7	35.0	7.9	72
13	*Diospyros sandwicensis*	W	4	-2.1177+15.9999*(1-exp(-0.1178*D))	0.80	2.0	1.7	53.9	15.8	36
14	*Eucalyptus robusta*	W	3	51.8735*(1-exp(-0.0181*D))	0.81	3.4	3.5	149.4	62.0	35
15	*Eucalyptus saligna*	W	3	63.2135*(1-exp(-0.0163*D))	0.78	4.6	8.6	149.0	71.0	89
16	*Falcataria moluccana*	W	1	exp(0.5900+0.6234*ln(D))*1.0559	0.88	0.8	1.2	188.7	54.6	136
17	*Ficus rubiginosa*	W	2	exp(0.7336+0.6960*ln(D)-0.0490*ln(D)^2)*1.0215	0.80	0.9	1.7	150.3	25.3	69
18	*Fraxinus uhdei*	W	2	exp(0.5863+0.8932*ln(D)-0.0585*ln(D)^2)*1.0109	0.97	1.3	2.1	165.0	35.9	107
19	*Grevillea robusta*	D	3	13.9201*(1-exp(-0.0682*D))	0.83	1.9	1.9	58.0	18.0	59
20	*Ilex anomala*	W	3	13.0821*(1-exp(-0.1339*D))	0.81	1.1	2.0	84.2	17.8	88
21	*Jacaranda mimosifolia*	D	3	8.7021*(1-exp(-0.0847*D))	0.63	5.3	2.4	42.4	9.7	30
22	*Metrosideros polymorpha*	D	3	14.1340*(1-exp(-0.0573*D))	0.63	2.6	2.2	98.3	21.5	129
23	*Metrosideros polymorpha*	W	3	22.9975*(1-exp(-0.0452*D))	0.90	1.0	1.4	98.3	33.3	664
24	*Myrsine lanaiensis*	D	4	1.9314+14.0107*(1-exp(-0.0238*D))	0.69	2.0	2.0	54.4	12.7	162
25	*Myrsine sandwicensis*	D	4	2.1002+8.1291*(1-exp(-0.0489*D))	0.55	3.4	2.8	43.0	11.5	17
26	*Perrottetia sandwicensis*	W	4	1.3360+11.8919*(1-exp(-0.0772*D))	0.79	0.5	1.3	16.2	11.6	90
27	*Pouteria sandwicensis*	D	3	13.2782*(1-exp(-0.0453*D))	0.26	20.1	6.0	49.8	14.2	31
28	*Prosopis pallida*	D	1	exp(0.3744+0.5194*ln(D))*1.0235	0.74	2.0	2.0	82.0	18.7	170
29	*Psidium cattleianum*	W	3	12.4891*(1-exp(-0.1569*D))	0.81	0.2	1.4	26.7	15.3	281
30	*Psychotria hawaiiensis*	W	3	9.2527*(1-exp(-0.1863*D))	0.53	0.8	1.5	19.9	12.8	63

31	*Psydrax odorata*	D	3	6.5422*(1-exp(-0.1832*D))	0.42	3.3	2.2	15.1	7.2	30
32	*Psydrax odorata*	W	3	7.4929*(1-exp(-0.2472*D))	0.75	0.8	1.9	9.6	8.7	44
33	*Santalum paniculatum*	D	1	exp(0.4386+0.3883*ln(D))*1.0265	0.49	2.2	2.3	25.2	8.0	29
34	*Sapindus saponaria*	D	3	10.7959*(1-exp(-0.0402*D))	0.31	20.7	5.2	62.8	12.2	29
35	*Schefflera actinophylla*	W	3	16.1354*(1-exp(-0.0800*D))	0.79	2.8	3.0	24.1	14.5	32
36	*Sophora chrysophylla*	D	3	5.3775*(1-exp(-0.2262*D))	0.29	2.4	1.9	24.1	8.5	34
37	*Trema orientalis*	W	4	0.7823+25.5680*(1-exp(-0.0258*D))	0.95	1.5	1.8	73.5	26.4	30
38	General Dry	D	2	$\exp(0.3480+0.6056*\ln(D)-0.0246*\ln(D)^2)*1.0514$	0.63	1.9	1.8	130.2	21.5	981
39	General Wet	W	2	$\exp(0.5120+0.7583*\ln(D)-0.0322*\ln(D)^2)*1.0409$	0.86	0.2	1.2	188.7	54.6	2257

WebTable 3. Estimates of wood density (WD, g cm^{-3}, oven-dried weight over green volume) by species or genus, assignment of diameter-to-AGB (aboveground biomass) and diameter-to-height models by species, and the frequency of species in the Hawaii database. Diameter-to-AGB models are found in WebTable 1, diameter-to-height models are found in WebTable 2. Wood density samples from the field were averaged from sections of at least six trees. Additional wood density values were taken from a global wood density database (Chave *et al.* 2009), and a default value of 0.5 g cm^{-3} was used when no field sample or literature value was available.

Species	Number of stems	WD	Diameter-to-AGB model[1]	Diameter-to-height model (wet)	Diameter-to-height model (dry)	Reference
Acacia koa	2247	0.55	1 (≤30cm dbh)	2	1	Field
Acacia melanoxylon	48	0.53		39	38	Chave
Aleurites moluccana	1	0.38		39	38	Chave
Antidesma platyphyllum	217	0.67		3	38	Field
Broussaisia arguta	1	0.21		39	38	Field
Casuarina equisetifolia	1110	0.81		4	38	Chave
Cecropia obtusifolia	40	0.31		5	38	Chave
Chamaesyce celastroides	10	0.50		39	38	Default
Chamaesyce olowaluana	208	0.50		39	38	Default
Charpentiera ovata	52	0.50		39	38	Default
Cheirodendron trigynum	2787	0.47		6	38	Field
Cibotium chamissoi	90	0.19	10	7	7	Field
Cibotium glaucum	942	0.22	10	8	8	Field
Cibotium menziesii	430	0.21	10	9	9	Field
Cibotium spp	182	0.21	10	10	10	Field
Coprosma pubens	1	0.48		11	38	Field
Coprosma rhyncocarpa	1	0.48		11	38	Field
Coprosma spp	1196	0.48		11	38	Field
Cyrtandra spp	3	0.50		39	38	Default
Diospyros sandwicensis	319	0.74		13	12	Field
Dodonea viscose	267	0.50	2	39	38	Default
Eucalyptus grandis	1	0.66		15	38	Chave
Eucalyptus robusta	1165	0.64		14	38	Chave
Eucalyptus saligna	801	0.74		15	38	Chave
Eucalyptus spp	399	0.83		15	38	Chave
Falcataria moluccana	5	0.43		16	38	Field
Ficus macrophylla	1	0.41		17	38	Chave
Ficus nota	76	0.41		39	38	Chave
Ficus rubiginosa	145	0.43		19	38	Field
Ficus spp	21	0.41		39	38	Chave
Flindersia brayleyana	39	0.48		39	38	Chave
Fraxinus uhdei	2445	0.48	7	18	38	Field
Grevillea robusta	1546	0.52		39	19	Chave
Hedyotis hillebrandii	51	0.38		39	38	Field
Hedyotis spp	75	0.38		39	38	Field
Hedyotis terminalis	15	0.38		39	38	Field
Ilex anomala	1466	0.48		20	38	Field
Jacaranda mimosifolia	19	0.49		38	21	Chave

Kokia drynarioides	7	0.50		39	38	Default
Melastoma septemnervium	5	0.46		39	38	Field
Melastoma spp	26	0.46		39	38	Field
Melicope clusifolia	103	0.50		39	38	Chave
Melicope pseudoanisata	19	0.50		39	38	Chave
Melicope spp	1	0.50		39	38	Chave
Melicope volcanica	8	0.50		39	38	Chave
Melochia umbellata	11	0.32		39	38	Chave
Metrosideros polymorpha	21373	0.69	3 (≤30cm dbh)	23	22	Field
Morella faya	3015	0.50	4	39	38	Chave
Morinda citrifolia	17	0.63		39	38	Chave
Myoporum sandwicense	2093	0.88		39	38	Chave
Myrsine lanaiensis	176	0.53		39	24	Field
Myrsine lessertiana	139	0.53		39	38	Field
Myrsine sandwicensis	16	0.53		39	25	Field
Myrsine spp	30	0.53		39	38	Field
Nestegis sanwicensis	6	0.50		39	38	Default
Nicotiana glauca	2	0.50		39	38	Default
Olea europaea	46	0.81		39	38	Chave
Osteomeles anthyllidifolia	4	0.50		39	38	Default
Pandanus tectorius	28	0.50		39	38	Default
Perrottetia sandwicensis	347	0.41		26	38	Field
Pipturus albidus	22	0.30		39	38	Field
Pisonia umbellifera	1	0.28		39	38	Chave
Pittosporum gayanum	1	0.61		39	38	Chave
Pleomele hawaiiensis	4	0.50		39	38	Default
Pouteria sandwicensis	13	0.69		39	27	Chave
Prosopis pallida	389	0.88	5	39	28	Chave
Psidium cattleianum	7616	0.69	6 (≤20cm dbh)	29	38	Field
Psidium guajava	41	0.65		39	38	Chave
Psychotria hawaiiensis	674	0.54		30	38	Field
Psydrax odorata	32	0.87		32	31	Chave
Sadleria spp	4	0.50		39	38	Default
Santalum paniculatum	22	0.72		39	33	Chave
Sapindus saponaria	126	0.71		39	34	Chave
Schefflera actinophylla	224	0.41		35	38	Chave
Schinus terebinthifolius	22	0.59		39	38	Chave
Sophora chrysophylla	692	0.64		39	36	Chave
Styphelia tameiameiae	107	0.50		39	38	Default
Syzygium cumini	2	0.67		39	38	Chave
Syzygium jambos	10	0.70		39	38	Chave
Toona ciliata	156	0.38		39	38	Chave
Trema orientalis	77	0.35		37	38	Chave
unknown	1680	0.50		39	38	Default
Wikstroemia spp	3	0.50		39	38	Default
Xylosma hawaiiense	1	0.66		39	38	Chave
Total number of stems:	57813					
Fraction with WD estimate:	90.66%					

[1]Models 8,9 used for all standing dead trees

WebTable 4. Forest type classifications based on GIS mapping of mean annual precipitation (MAP) and mean annual temperature (MAT). Units for precipitation and temperature are represented in millimeters and ^{o}C, respectively.

Class name	MAP/MAT regions
Moist-Montane	1500 < MAP < 3500 and MAT < 18
Moist-Lowland	1500 < MAP < 3500 and MAT > 18
Dry-Montane	MAP < 1500 and MAT < 18
Dry-Lowland	MAP < 1500 and MAT > 18
Wet-Montane	MAP > 3500 and MAT < 18
Wet-Lowland	MAP > 3500 and MAT > 18

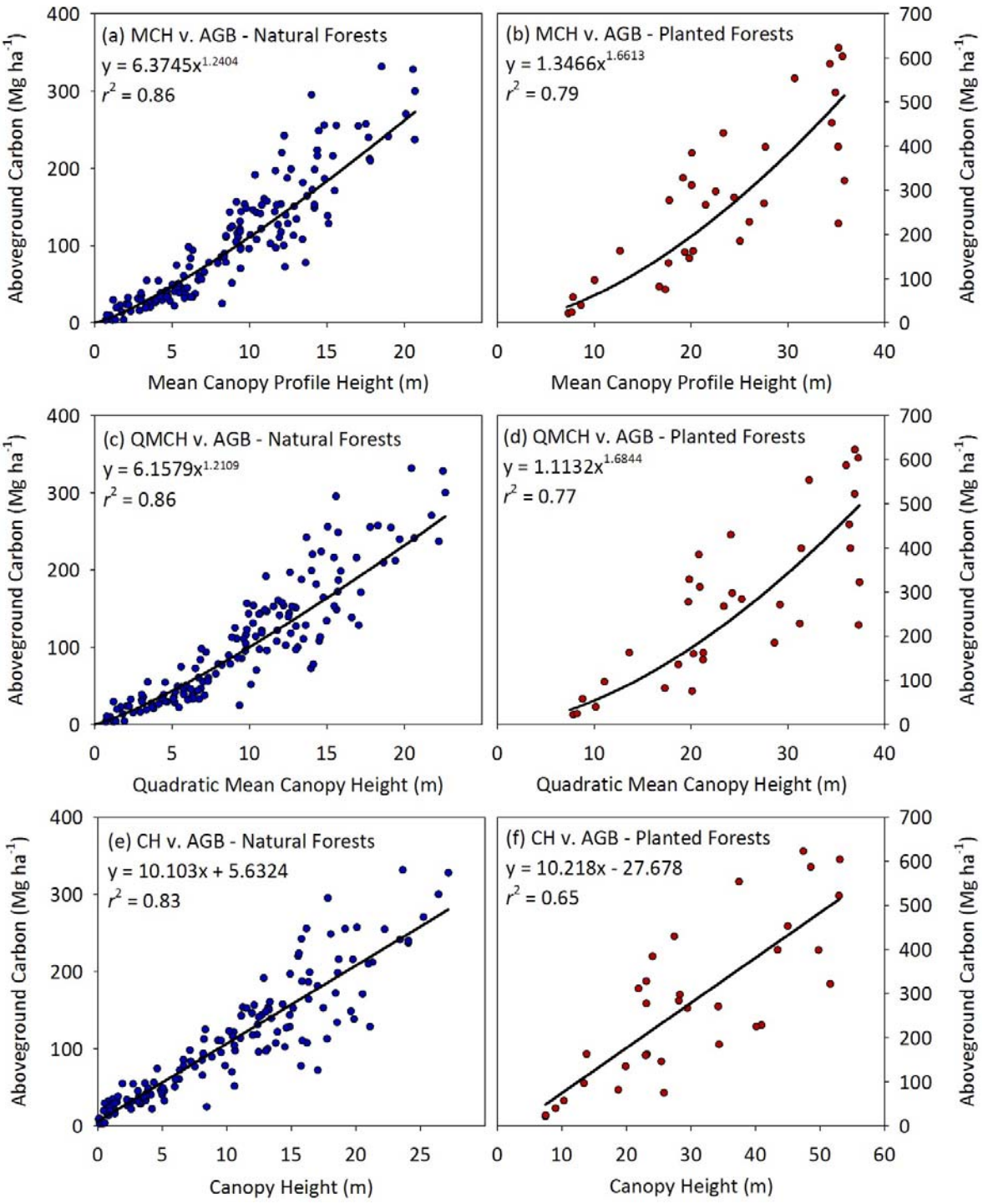

WebFigure 1. Relationships between various LiDAR-derived metrics and aboveground carbon density for natural and planted forests (Mg C ha^{-1}). MCH is mean canopy profile height, QMCH is quadratic mean canopy height, and CH is top-of-canopy height (described by Lefsky *et al.* 2002).

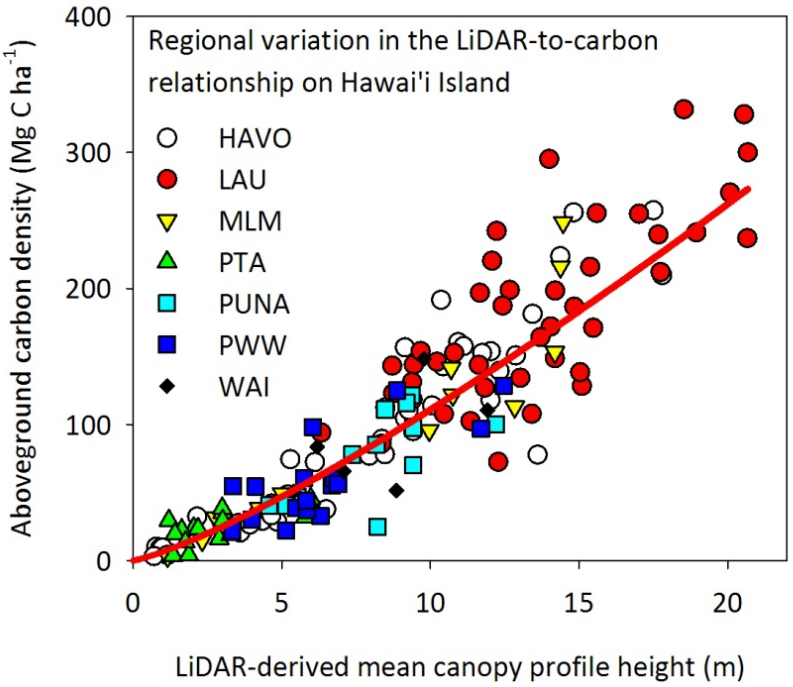

WebFigure 2. Relationship between LiDAR-derived mean canopy profile height and plot-level aboveground carbon (C) density. The model was highly significant ($p < 0.0001$) and explained C density variation among seven distinct physiographic provinces in Hawaii: savannas and successional forests in Hawaii Volcanoes National Park (HAVO), dense closed-canopy forest in the Laupahoehoe section of the Hilo Forest Reserve (LAU), a successional gradient along the Mauna Loa Matrix (MLM), savannas and dry forest in the Pohakuloa Training Area (PTA), wet native and introduced successional forests in Puna (PUNA), savannas and dry forests in Pu'u Waa' Waa' (PWW), and closed-canopy forests of introduced trees in the Waiakea Management Area (WAI).

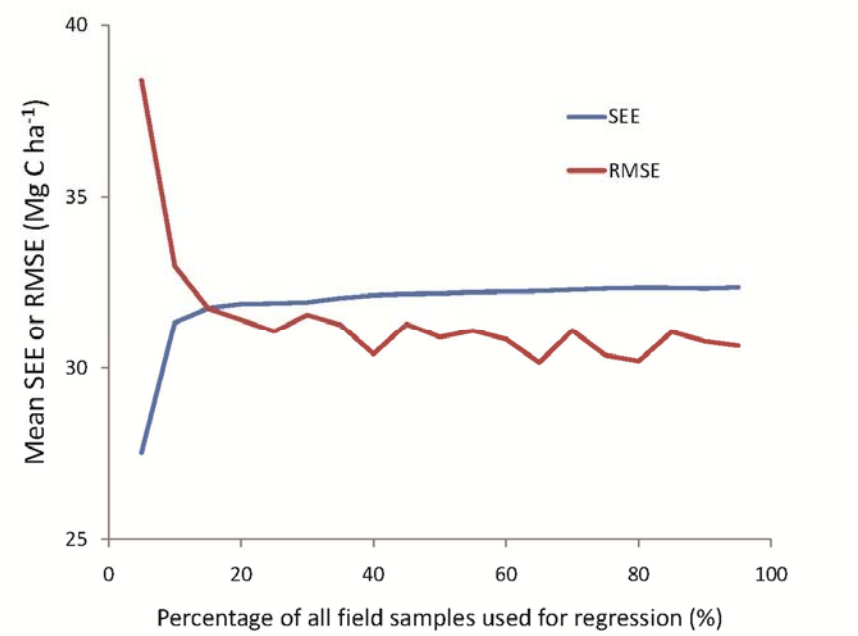

WebFigure 3. Error analysis of LiDAR-to-carbon relationship.

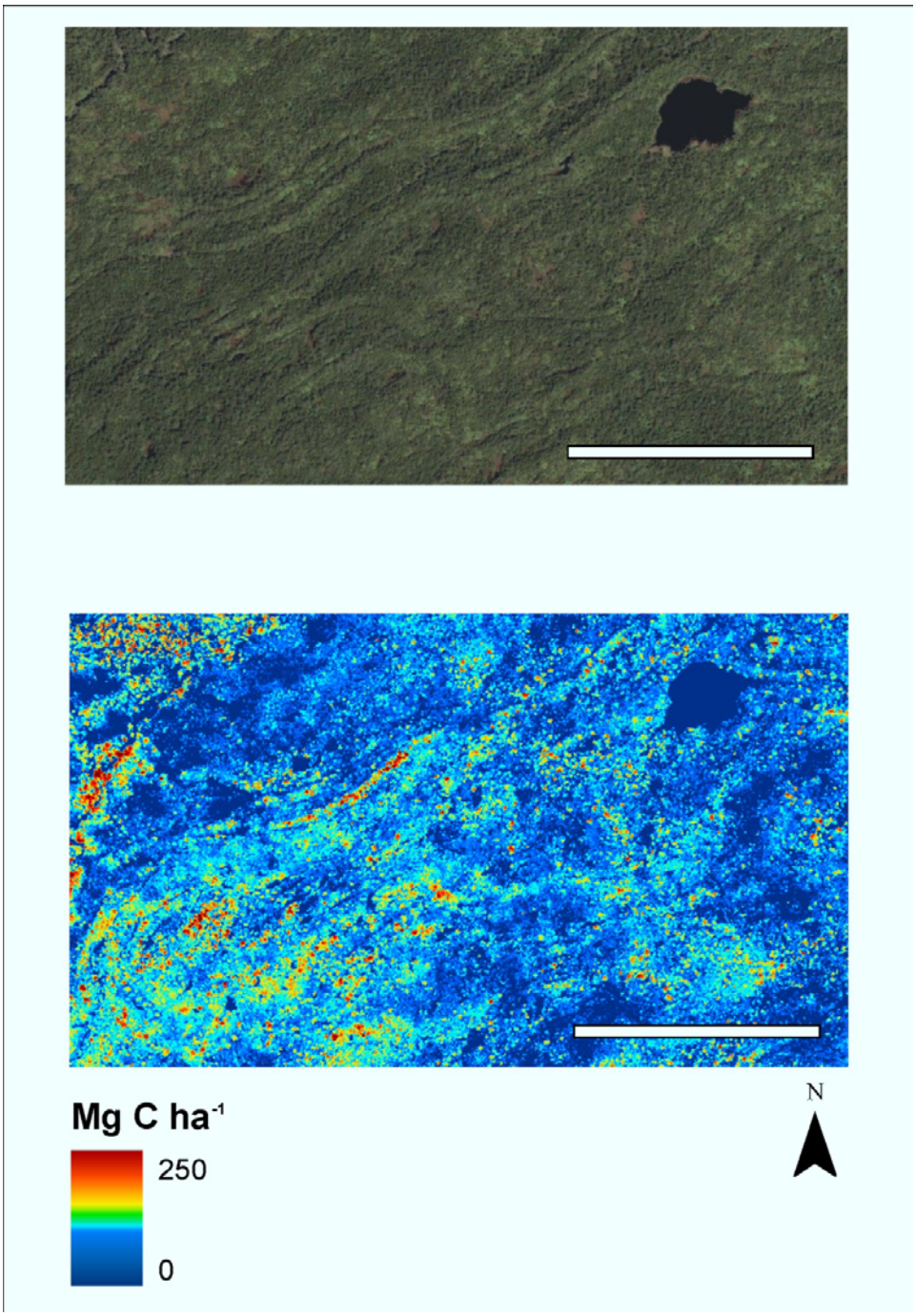

WebFigure 4. Hawaiian rainforests within the Hakalau National Wildlife Refuge as seen by Google Earth (top), compared with LiDAR-based carbon mapping (bottom). The white bars indicate 500 m of distance.

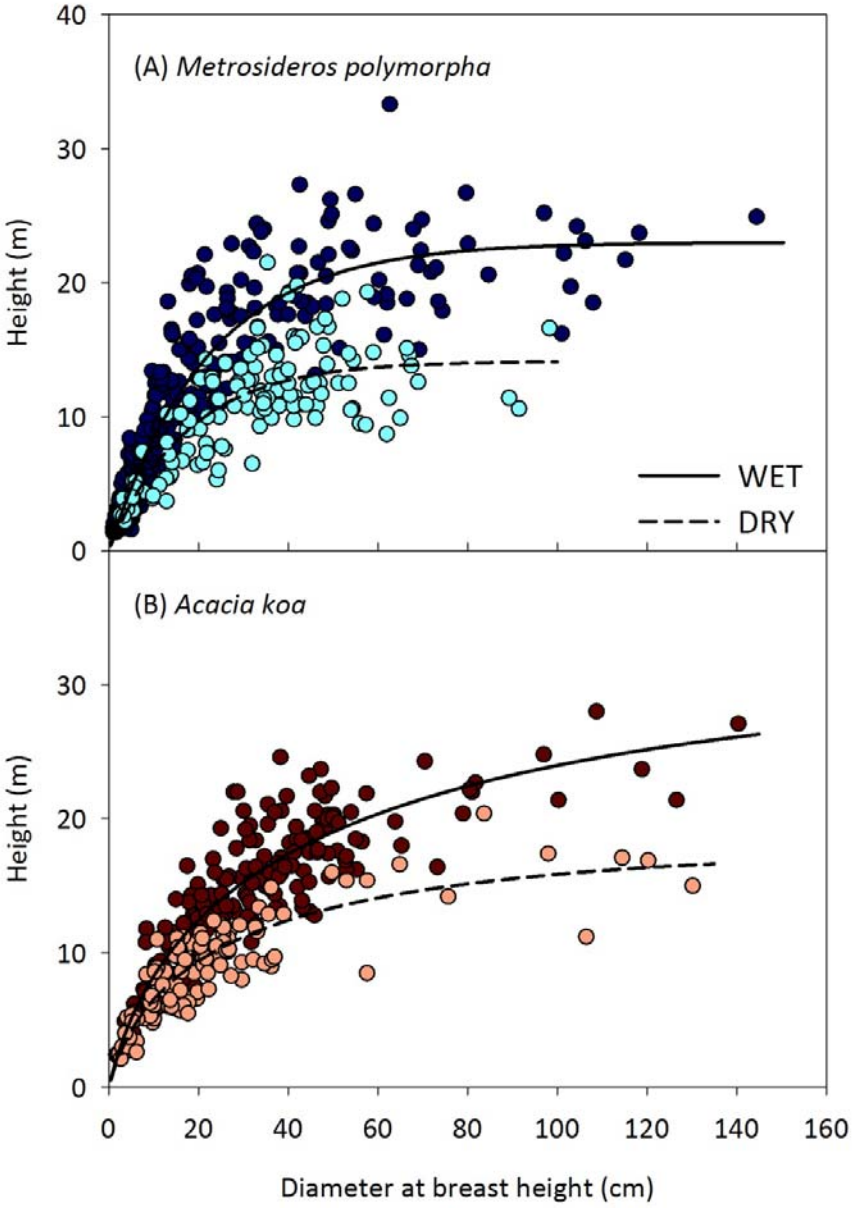

WebFigure A1. Diameter-to-height relationships for the two most common native tree species on Hawaii Island: (A) *Metrosideros polymorpha*, and (B) *Acacia koa*. As with two additional species not shown (*Diospyros sandwicensis*, *Psydrax odorata*), height increased more steeply with diameter in ecosystems on the wet side of the island.

WebReferences

Aboal JR, Arevalo JR, and Fernandez A. 2005. Allometric relationships of different tree species and stand above ground biomass in the Gomera laurel forest (Canary Islands). *Flore* **200**: 264–74.

Asner GP, Broadbent EN, Oliveira PJC, *et al.* 2006. Condition and fate of logged forests in the Brazilian Amazon. *Proceedings of the National Academy of Sciences* **103**: 12947–50.

Asner GP, Elmore AJ, Hughes FR, *et al.* 2005. Ecosystem structure along bioclimatic gradients in Hawaii from imaging spectroscopy. *Remote Sensing of Environment* **96**: 497–508.

Baskerville G. 1972. Use of logarithmic regression in the estimation of plant biomass. *Canadian Journal of Forest Research-Revue Canadienne De Recherche Forestiere* **2**: 49–53.

Broadbent EN, Asner GP, Keller M, *et al.* 2008. Forest fragmentation and edge effects from deforestation and selective logging in the Brazilian Amazon. *Biological Conservation* **141**: 1745–57.

Chave J, Andalo C, Brown S, *et al.* 2005. Tree allometry and improved estimation of carbon stocks and balance in tropical forests. *Oecologia* **145**: 87–99.

Chave J, Coomes D, Jansen S, *et al.* 2009. Towards a worldwide wood economics spectrum. *Ecology Letters* **12**: 351–66.

FAO (Food and Agriculture Organization of the United Nations). 2000. Global Forest Resources Assessment 2000. Rome, Italy: Food and Agriculture Organization. www.fao.org/DOCREP/004/Y1997E/Y1997E00.HTM. Viewed 25 Jan 2011.

Giambelluca TW, Nullet MA, and Schroeder TA. 1986. Rainfall atlas of Hawaii. Honolulu, HI: State of Hawaii, Department of Land and Natural Resources, Division of Water and Land Development.

Gibbs HK, Brown S, Niles JO, and Foley JA. 2007. Monitoring and estimating tropical forest carbon stocks: making REDD a reality. *Environmental Research Letters* **2**: 1–13.

GLC. 2000. Global Land Cover Database. Ispra, Italy: European Commission, Joint Research Centre.

Hughes RF, Kauffman JB, and Jaramillo VJ. 1999. Biomass, carbon, and nutrient dynamics of secondary forests in a humid tropical region of Mexico. *Ecology* **80**: 1892–907.

IPCC (Intergovernmental Panel on Climate Change). 2006. Guidelines for National Greenhouse Gas Inventories. Kyoto, Japan: National Greenhouse Gas Inventories Programme.

Lefsky MA, Cohen WB, Parker GG, and Harding DJ. 2002. Lidar remote sensing for ecosystem studies. *BioScience* **52**: 19–30.

Litton CM and Kauffman JB. 2008. Allometric models for predicting aboveground biomass in two widespread woody plants in Hawaii. *Biotropica* **40**: 313–20.

Litton CM, Sandquist DR, and Cordell S. 2006. Effects of non-native grass invasion on aboveground carbon pools and tree population structure in a tropical dry forest of Hawaii. *Forest Ecology and Management* **231**: 105–13.

Mascaro J, Becklund KK, Hughes RF, and Schnitzer SA. 2008. Limited native plant regeneration in novel, exotic-dominated forests on Hawaii. *Forest Ecology and Management* **256**: 593–606.

Niklas KJ. 1995. Size-dependent allometry of tree height, diameter and trunk-taper. *Annals of Botany* **75**: 217–27.

Nogueira EM, Fearnside PM, Nelson BW, *et al.* 2008. Estimates of forest biomass in the Brazilian Amazon: new allometric equations and adjustments to biomass from wood-volume inventories. *Forest Ecology and Management* **256**: 1853–67.

Padron E and Navarro RM. 2004. Estimation of above-ground biomass in naturally occurring populations of *Prosopis pallida* (H. & B. ex. Willd.) H.B.K. in the north of Peru. *Journal of Arid Environments* **56**: 283–92.

Wagner WL, Herbst DR, and Sohmer SH. 1999. Manual of the flowering plants of Hawaii. Honolulu, HI: University of Hawaii Press/Bisphop Museum Press.

Zimmerman N, Hughes RF, Cordell S, *et al.* 2008. Patterns of primary succession of native and introducted plants in lowland wet forests in Eastern Hawaii. *Biotropica* **40**: 277–84.